Journal of Materials Chemistry C

Accepted Manuscript

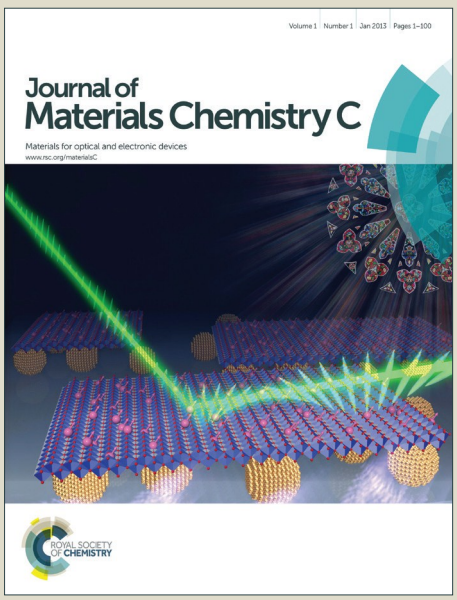

ROYAL SOCIETY OF CHEMISTRY

www.rsc.org/materialsC

Journal Name

ARTICLE TYPE

Cite this: DOI: 10.1039/xxxxxxxxxx

Enhanced Piezoelectricity and Half-metallicity of Fluorinated AlN Nanosheet and Nanoribbons: A First-principles Study

Yi Ding*[a], and Yanli Wang *[b]

Received Date
Accepted Date

DOI: 10.1039/xxxxxxxxxx

www.rsc.org/journalname

Utilizing first-principles calculations, we have investigated the structural, mechanical, piezoelectric, and electronic properties of fluorinated AlN (F-AlN) nanosheet and nanoribbons. Unlike the fluorinated graphene and BN systems, the F-AlN sheet favours a stable boat-like buckled structure, which has a soft mechanical feature with anisotropic Young modulus and Poisson ratio. Such structural flexibility and anisotropy result in an improved piezoelectric performance for the F-AlN system, whose piezoelectric coefficients, especially d_{11} and e_{11}, are larger than those of hexagonal group III-V, group-III monochalcogenide, and transition metal dichalcogenide nanosheets. The F-AlN sheet and its armchair nanoribbons are semiconductors, while the zigzag ones become metallic. Particularly, an intriguing half-metallic behaviour appears in these zigzag F-AlN nanoribbons, whose half-metal gaps are large for room-temperature operation. Moreover, armchair F-AlN nanoribbons can also be converted to half-metals by the hole doping, which brings tunable half-metal gaps to the system. Our study demonstrates that fluorination is an efficient route to tailoring the properties of AlN nanomaterials, which have promising piezoelectric performance and half-metallic characteristics for the potential applications in nano-sized energy harvesting and spintronic devices.

1 Introduction

Since the successful preparation of graphene, two-dimensional (2D) inorganic nanosheets, such as BN, AlN, SiC, ZnO, and MoS_2 ones, have attracted extraordinary amount of interests from both academia and industry[1–4]. Among them, the AlN nanostructure is a promising material due to its wide applications in optics, electronics, and photoelectronics[5–7]. For example, because of the good structural stability, moderate piezoelectricity, and high signal-to-noise ratio, AlN thin films have been used as piezoelectric accelerometers and resonators in the experiments[8–10]. Very recently, by the molecular beam epitaxy, monolayer and few-layer AlN nanosheets have been successfully synthesized on the Ag(111) and Si(111) surfaces[11,12]. The formed AlN monolayer is a flat hexagonal sheet akin to graphene, which has a large band gap due to the elemental difference between two sublattices of hexagons[13–15]. Theoretical studies have shown the induction of defects and strains can effectively modify the gap size of AlN nanosheet[16,17]. By first-principles calculations, it has been found that the Al and N vacancies can induce a half-metal behaviour in the AlN sheet, which possesses a ferromagnetic property with high Curie temperatures above room temperature[18]. Besides the 2D sheet, one-dimensional (1D) ribbon form has also been reported for the AlN nanostructure in the experiment[19]. First-principles calculations have found that all the zigzag and armchair AlN nanoribbons are nonmagnetic semiconductors when the dangling bonds of edges are passivated[18,20]. Through tuning the edge passivations, diverse electronic and magnetic properties would appear in the zigzag AlN nanoribbons, which can become ferromagnetic semiconductors when only the Al edge is H-passivated while change to antiferromagnetic semiconductors if the single N edge is H-passivated[21]

[a] Department of Physics, Hangzhou Normal University, Hangzhou, Zhejiang 310036, People's Republic of China. E-mail: dingyi2001@tsinghua.org.cn
[b] Department of Physics, Center for Optoelectronics Materials and Devices, Zhejiang Sci-Tech University, Xiasha College Park, Hangzhou, Zhejiang 310018, People's Republic of China. E-mail: wangyanli-04@tsinghua.org.cn

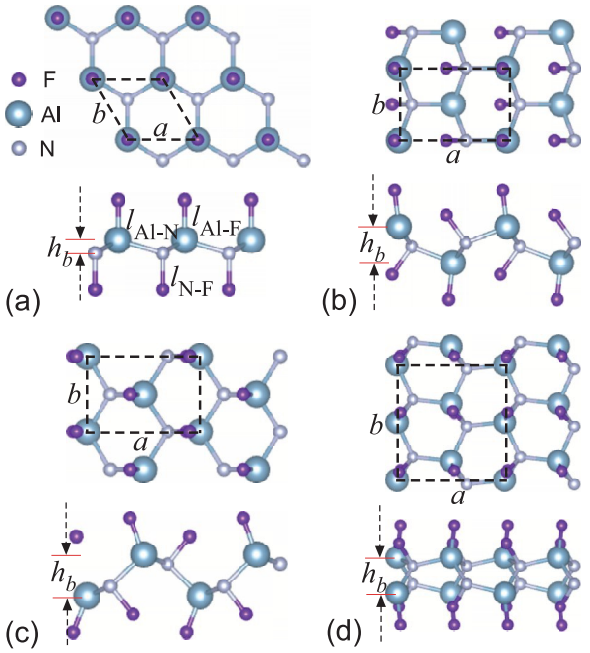

Fig. 1 The top and lateral view of (a) chair, (b) boat, (c) Z-line, (d) A-line conformations for the F-AlN sheet.

When the edge atoms are bare, the intrinsic half-metallicity in zigzag AlN nanoribbons can be further modulated, which could be converted to metals/semiconductors by foreign electric field and strain[22]. While for armchair AlN nanoribbons, diverse electric and magnetic properties can be obtained by different edge terminations[23–25].

Nowadays, covalent functionalization becomes an effective way to tailor the properties of nanostructures[26,27]. Experimentally, reversible hydrogenation has been realized on graphene by H-plasma processing, which yields a buckled chair-like conformation[28]. Analogous fluorinated graphene and BN sheets have also been fabricated in the experiments[29–31]. It has been found that the hydrogenation and fluorination bring versatile electronic, piezoelectric and magnetic properties into the nanosheets[32–38]. Similar to the hydrogenated case, the fully fluorination also transforms graphene from a semimetal to an insulator, and for the fluorographene nanoribbons, the electronic properties can be well tuned by edge chemical modification and the fluorinated width, which may produce a half-metallic to half-semiconducting transition in zigzag hybrid nanoribbons[39]. Unlike graphene, the H or F surface decorations on BN sheets reduce the band gap, and the functionalized BN sheets can lead to a tunable doping behaviour and a sizeable band gap in the supported graphene layer[40]. Regarding to the AlN sheet, two-side hydrogenation on the surface enlarges the band gap, while one-side hydrogenation at the Al site transforms it into a p-type ferromagnetic semiconductor[41–43].

When the AlN sheet is co-decorated by H and F atoms on both sides, an anisotropic semiconducting character will appear, which is useful for the applications in sensors and solar cells[43]. Unlike the monolayer structure, the hydrogen adsorptions on multilayer AlN sheets favour the N sites instead, and the corresponding semi-hydrogenated system can be magnetic semiconductors, half-metals or metals depending on the thickness of nanosheets[44]. A half-metallic behaviour has also been reported in the one-side-fluorinated AlN sheet, which adopts the same structural conformation as the hydrogenated one[45,46]. However, so far, the two-side fluorination on AlN sheet has not been systematically investigated yet. It would be noticed that previous studies on the functionalized AlN sheets are limited to the chair conformation. Normally, the surface functionalization will bring different conformations into the nanosheets[47,48]. Thus, several interesting questions arise: which one is the most favourable conformation for the fluorinated AlN sheet? What are the peculiar properties brought by fluorination into AlN sheet? What about the electric and magnetic properties of their corresponding nanoribbons? To address these issues, we have conducted a comprehensive first-principles calculations on the structural, mechanical, piezoelectric, electronic and magnetic properties of fluorinated AlN nanostructures.

2 Methods

The first-principles calculations are performed by the VASP code[49,50], which utilizes the plane-wave basis sets with an energy cut-off of 600 eV and Perdew-Burke-Ernzerhof (PBE) projector-augmented wave pseudopotentials. The van der Waals corrections have been considered by the semiempirical DFT-D3 method with Becke-Jonson damping[51,52], and dipole corrections have also been employed in the calculations to account for the possible dipole moments in the fluorinated nanostructures. In order to simulate the isolated case, a vacuum layer of about 15 Å is used to avoid spurious interactions between replicas. The Brillouin zone is sampled by a $21 \times 31 \times 1$ **k**-mesh grid for nanosheets, which changes to the $1 \times 8 \times 1$ one for nanoribbons. The lattice constants and atomic coordinates are fully relaxed until the force on each atom is less than 3×10^{-3} eV/Å and the total energy changes are less than 10^{-5} eV. In addition to the PBE calculation, the hybrid functional of Heyd-Scuseria-Ernzerhof (HSE) has been used to obtain more accurate band gaps. The HSE calculations are done by the FHI-aims code[53], which adopts the HSE06 form with a screening parameter of 0.11 bohr^{-1}. The dynamic stabilities of fluorinated nanosheets are checked by phonon calculations, which is performed by the Phonopy code[54,55].

3 Results and discussions

Structures and Stabilities

For the two-side fluorinated AlN (F-AlN) sheet, four isomeric conformations have been considered as the possible structures as

System	a (Å)	b (Å)	l_{Al-N} (Å)	l_{Al-F} (Å)	l_{N-F} (Å)	h_b (Å)	E_f (eV/F)
AlN	3.12	=a	1.80	–	–	0	–
chair F-AlN	3.19	=a	1.93	1.65	1.49	0.57	-2.129
boat F-AlN	4.86	3.24	1.94,1.98	1.65	1.52	1.62	-2.206
A-line F-AlN	5.32	5.70	1.93,1.95	1.65	1.52	1.79	-2.183
Z-line F-AlN	4.80	3.20	1.93,1.93	1.65	1.51	1.74	-2.189

Table 1 The structural parameters for the pristine and fluorinated AlN sheets. a and b are the two lattice constants, l_{Al-N}, l_{Al-F}, and l_{N-F} are the Al-N, Al-F, and N-F bond lengths. h_b is the buckling height of the AlN basal plane as denoted in Fig. 1(a). All these structural parameters are in the unit of Å. E_f is the formation energy of the fluorinated AlN sheet in the unit of eV/F.

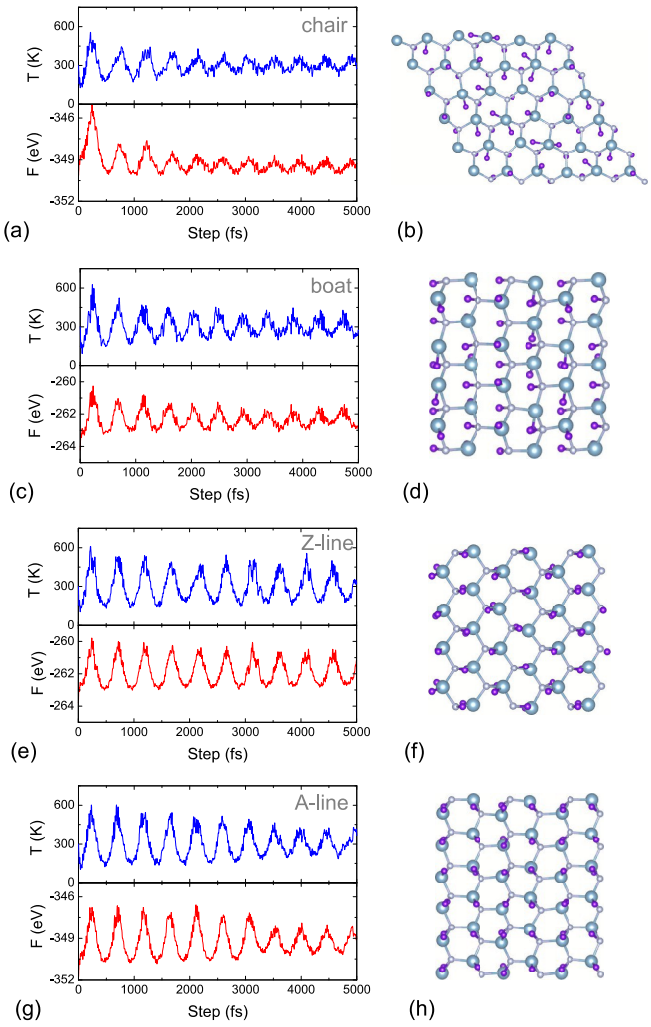

Fig. 2 The fluctuations of temperature and energy with time for (a) chair, (c) boat, (e) Z-line, and (g) A-line configurations at $T = 300K$. The structures in (b) chair, (d) boat, (f) Z-line, and (h)A-line correspond to their final structures after 5000 time steps.

shown in Fig. 1. Following the convention of literature[48,56], they are referred to as the chair, boat, Z-line and A-line conformations in the paper. Here, in the chair conformation, F atoms are attached to Al and N atoms alternatively on the opposite sides of sheet, while in the boat conformation, they are attached to Al-N pairs alternatively. In the A-line and Z-line conformations, the F atoms are alternatively arrayed on the Al-N armchair and zigzag lines, respectively. Table 1 lists the optimized structural parameters for these conformations. It shows the Al-F bond length is always 1.65 Å, while the N-F bond length is varied from 1.49 to 1.52 Å in these F-AlN sheets. The Al and N atoms undergo a sp^2-to-sp^3 transition upon the fluorination, which causes a puckered structure with a buckling height of 0.57, 1.62, 1.74, and 1.79 Å in the chair, boat, Z- and A-line conformations, respectively. It elongates the Al-N bond lengths from 1.80 Å in pristine AlN sheet to 1.93∼1.98 Å in the fluorinated structure, which will weaken the in-plane stiffness as discussed below.

The formation energies of F-AlN sheets, defined as $E_f = E_{F-AlN} - E_{AlN} - n_F E_{F_2}/2$, are used to determine the energetic stabilities of different conformations. Here, E_{F-AlN} and E_{AlN} are the total energies of fluorinated and pristine AlN sheets, E_{F_2} is the energy of an isolated F_2 molecule and n_F is the number of F atoms in the compound. By this definition, a more negative E_f means a stronger stability of the conformation. As shown in Tab. 1, all the F-AlN sheets have negative formation energies of -2.1∼-2.2 eV/F, which are comparable to the fluorinated graphene (-2.04 eV/F)[57] and BN systems (-2.50 eV/F)[58]. The E_f of different conformations are found to follow the sequence of boat < Z-line < A-line < chair, which indicates the boat conformation is the most stable structure for F-AlN sheet, while the chair one is the least favourable structure.

To examine the thermal stabilities of these structures, we have performed ab initio molecular dynamics (AIMD) simulations on these F-AlN sheets. A Nosé thermostat of 300 K and a time step of 1 fs are used in the AIMD calculations, and the large supercells of $4\times4\times1$, $2\times3\times1$, $2\times3\times1$, and $2\times2\times1$ units are adopted for the chair, boat, Z-line and A-line configurations, respectively. Figure 2 depicts the fluctuations of energy and temperature with time

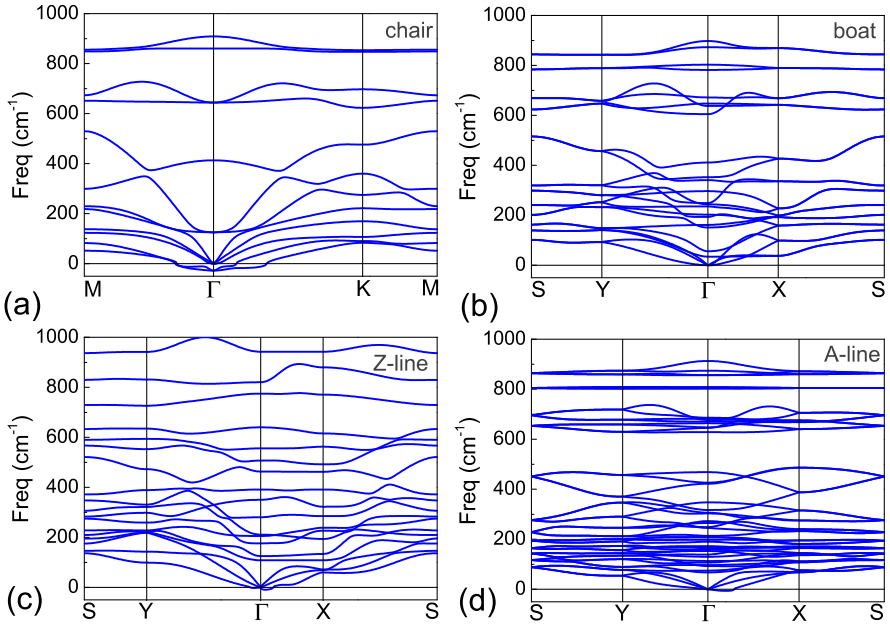

Fig. 3 The phonon dispersions of (a) chair, (b) boat, (c) Z-line, and (d) A-line conformations.

and the final structures for these F-AlN sheets. It can be seen that after 5000 steps, their structural integrities and buckling configurations are still maintained. Although some displacements of F atoms are noticeable in the chair configuration, they are smaller in the boat, Z-line and A-line ones and can be optimized back to the initial structures after a full structural relaxation. There are no breakages in the Al-N skeletons, which demonstrates these fluorinated sheets are thermally stable at room temperature. For the boat configuration, we further perform the AIMD simulations under 500, 800, 1000 K, and find the structure can be kept at 500 K but becomes broken at higher temperatures of 800 and 1000 K. Thus, the AIMD simulations prove the fluorinated AlN sheets will possess good structural stabilities at room temperature, which is beneficial for their practical applications in nano-devices.

A phonon calculation is performed to further check the structural stabilities of these conformations. As shown in Fig. 3(a), the chair conformation has a noticeable soft mode with the negative frequency of -27 cm^{-1} at the Γ point. The eigenvector analysis shows such soft mode would lead to large deformations of Al-F bonds. For the Z-line and A-line conformations, although the soft modes disappear at the Γ points, a negative frequency of about 10 cm^{-1} appears in the vicinity of Γ point. This suggests that both conformations will suffer from a phonon instability owing to the long wavelength acoustic vibrations. Only the boat conformation possesses a robust phonon stability without soft modes. As shown in Fig. 3(b), throughout the whole Brillouin zone, there are no negative frequencies in the phonon dispersion curves, which verifies that the energetically favourable boat conformation is also dynamically stable. Therefore, when the AlN sheet has been fluorinated, the boat-like buckled structure is the most possible conformation, for which the detailed physical properties are investigated as follows.

Mechanical and Piezoelectric Properties

Firstly, we investigate the mechanical characteristics of F-AlN sheet. Due to the orthorhombic symmetry of boat conformation, the elastic energies can be expressed as $U(\varepsilon) = C_{11}\varepsilon_1^2/2 + C_{22}\varepsilon_2^2/2 + C_{12}\varepsilon_1\varepsilon_2 + 2C_{66}\varepsilon_6^2$ under small strains. Here, Voigt notation is adopted for strains, for which the indexes are numbered as $1 \to xx$, $2 \to yy$, $3 \to zz$, $4 \to yz$, $5 \to xz$, $6 \to xy$. Utilizing the energy-vs.-strain method[59,60], we obtain $C_{11} = 48.4, C_{22} = 81.7, C_{12} = 23.3, C_{66} = 31.8$ N/m for the F-AlN sheet. For comparison, the elastic constants of AlN sheet are also calculated as $C_{11} = C_{22} = 152.3, C_{12} = 59.6, C_{66} = (C_{11} - C_{12})/2 = 46.4$ N/m by the same method, which are consistent with previous results of $C_{11} = 156.7, C_{12} = 57.4$ N/m by Peng *et al.*[61]. Evidently, the elastic constants of F-AlN sheet become smaller than those of the pristine counterpart. Due to the buckled structure, C_{11} and C_{22} are no longer equivalent in the F-AlN sheet, which leads to an anisotropic mechanical feature as characterized by a non-isotropic Young modulus E and Poisson ratio ν. Using the obtained elastic constants, the E and ν along an arbitrary direction θ (θ is the angle

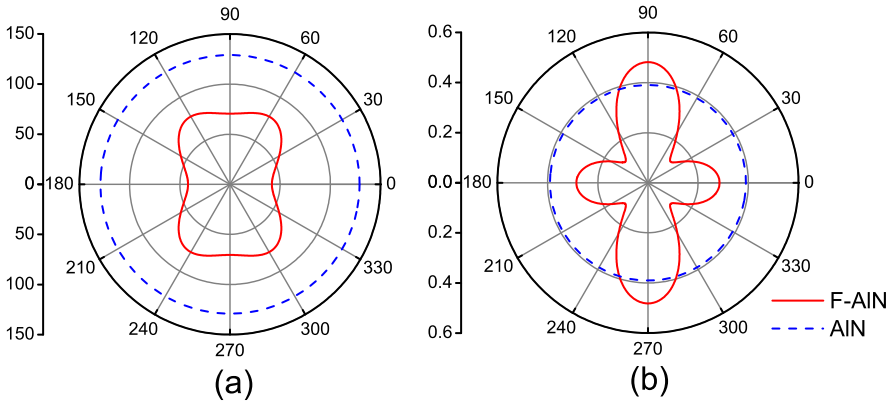

Fig. 4 The polar diagrams of the in-plane (a) Young modulus E and (b) Poisson ratio ν along an arbitrary direction for AlN and F-AlN sheets. The solid curves correspond to the F-AlN sheet, while the dashed circles in the polar diagrams correspond to the pristine AlN sheet.

relative to the positive x direction) are computed as

$$E(\theta) = \frac{C_{11}C_{12} - C_{12}^2}{C_{11}s^4 + C_{22}c^4 + (\frac{C_{11}C_{12}-C_{12}^2}{C_{66}} - 2C_{12})c^2s^2}$$

$$\nu(\theta) = -\frac{(C_{11} + C_{22} - \frac{C_{11}C_{12}-C_{12}^2}{C_{66}})c^2s^2 - C_{12}(c^4 + s^4)}{C_{11}s^4 + C_{22}c^4 + (\frac{C_{11}C_{12}-C_{12}^2}{C_{66}} - 2C_{12})c^2s^2}$$

, where $c = cos\theta$ and $s = sin\theta$ [59,60]. The corresponding polar diagrams of $E(\theta)$ and $\nu(\theta)$ are depicted in Fig. 4 for both F-AlN and AlN sheets. Note that the E and ν of AlN sheet (129.0 N/m and 0.39) are independent on the angle θ due to its isotropic feature. Hence they have circular shapes in the polar diagram. On the other hand, the E and ν of F-AlN sheet are quite orientation-dependent, which deviate from the circular shape owing to the anisotropy. The maximum and minimum Poission ratio are 0.48 and 0.12 at $\theta = 90.0^\circ$ and 43.0°, respectively. For the Young modulus, the maximum and minimum values are 78.1 and 41.8 N/m at $\theta = 59.3^\circ$ and 0.0°, which are only 61% and 32% of that in the AlN sheet. It indicates that the F-AlN sheet is much softer than the pristine structure. Similar phenomena have also been reported in the hydrogenated and fluorinated graphene systems [59,62]. The reduced in-plane stiffness is related to the structural changes by surface decoration. On one hand, the distance between Al and N atoms is elongated upon fluorination, which causes the weakening of Al-N bonds in the F-AlN sheet. On the other hand, the F-AlN basal plane becomes buckled, which pronouncedly increases the out-of-plane flexibility. Thus, after the fluorination, the AlN sheet becomes a structurally anisotropic nanomaterial with softer mechanical features.

For the F-AlN sheet, the enhanced structural flexibility would facilitate its piezoelectric performance. According to the orthorhombic $Pmn2_1$ space group of fluorinated structure, three non-zero piezoelectric stress coefficients e_{11}, e_{12} and e_{26} need to be calculated. Based on the Maxwell relation of $e_{ij} = \partial P_i/\partial \varepsilon_j$ these piezoelectric coefficients can be obtained by linear fitting of the polarization change-vs.-strain curve [63,64]. Here, the calculation of e_{11} requires to apply strains (ε_1) along the armchair direction, the e_{12} and e_{26} ones need to apply strains of ε_2 and ε_6 along the zigzag and shear directions, respectively. Under each strain, the lattice constants are fixed while the internal atomic positions are fully relaxed. The polarization of structure is calculated by the modern Berry phase method [65,66]. Figure 5(a) depicts the polarization change versus the applied strain in a small strain range of [-0.01, 0.01], which shows a linear relationship between them. The slope gives the piezoelectric stress coefficients as $e_{11} = -1104$, $e_{12} = 333$ and $e_{26} = -623$ pC/m, which are much larger than the value of pristine AlN sheet ($e_{11} = 233$ pC/m by our calculation and 223 pC/m in the literature [63]). The corresponding piezoelectric strain coefficients d_{ij} can be obtained from the inversion of transformation relationship of $e_{ij} = \sum_{k=1}^{6} d_{ik}C_{kj}$. Based on the calculated C and e values, we obtain the F-AlN sheet has $d_{11} = -28.67$, $d_{12} = 12.25$, and $d_{26} = -19.58$ pm/V which are also remarkably larger than the pristine AlN counterparts ($d_{11} = -2.51$, $d_{12} = 2.51$, $d_{26} = 5.03$ pm/V by our calculation). It is worth noting that the piezoelectric strain coefficients d_{11} of F-AlN sheet are larger than the values of normal 2D piezoelectric materials, which are only $0.02 - 5.5$ pm/V in hexagonal group III-V nanosheets [63], 1.46−2.30 pm/V in layered group-III monochalcogenides [67], 2.19−9.13 pm/V in monolayer transition metal dichalcogenides [68], and about 1 pm/V in the F/H-decorated BN nanosheets [58]. Very recently, Li *et al.* have found the orthorhombic GeSe, SnS and SnSe sheets possess giant piezoelectricity up to the order of 10^2 pm/V [69]. Here, the enhancement of d_{11} in the F-AlN sheet shares the same cause which is attributed to the special C_{2v} symmetry of the buckled structure. Different from the hexagonal lattices, whose $d - e$ relation is $d_{11} = e_{11}/(C_{11} - C_{22})$, the orthorhombic lattice will have

$d_{11} = (e_{11}C_{22} - e_{12}C_{12})/(C_{11}C_{22} - C_{12}^2)$. Here, the opposite sign of e_{11} and e_{12}, the small C_{11} and large C_{12} values, cause a big d_{11} value in the F-AlN sheet. Such large piezoelectric coefficients would render the F-AlN nanomaterials several intriguing applications in nano-sized piezoelectric sensors, resonators, and energy harvesting nano-devices.

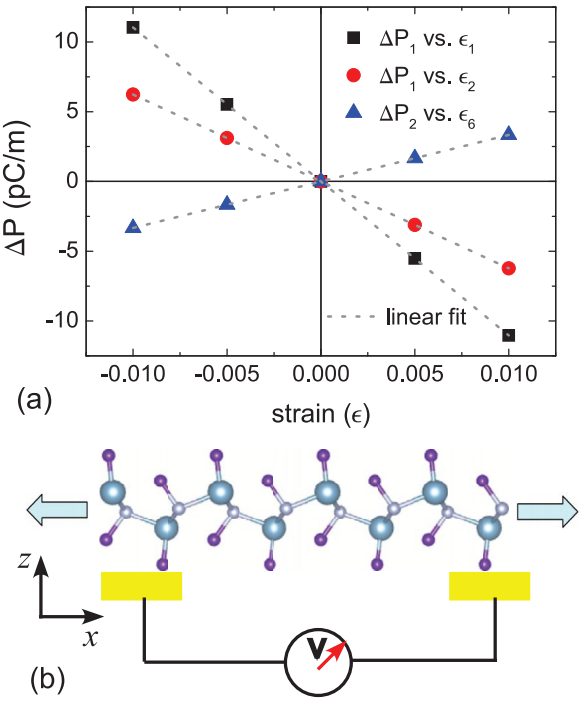

Fig. 5 (a) The polarization change as a function of uniaxial strains for the F-AlN sheet.(b)The schematic diagram of the voltage output at the sample edges of the strained F-AlN sheet.

Besides that, it would be noted that the e_{11} of F-AlN sheet is also big, which is comparable to that of GeSe sheet (about 1.23×10^3 pC/m)[69]. To compare with bulk materials, a scaled $e_{11,3D}$ in the unit of C/m^2 is obtained from dividing the two-dimensional value by its thickness. Following the previous study[37], the thickness of F-AlN sheet is approximate to the height between the top and bottom F atoms (4.90 Å) plus one Al-F bond length (1.65 Å), which is equal to 6.55 Å. For the F-AlN sheet, the corresponding $e_{11,3D}$ is 1.69 C/m^2, which is one order of magnitude larger than that of α-quartz (0.171 C/m^2)[70] and about four times of the value in the langasite (-0.397 C/m^2)[71]. Utilizing this giant piezoelectric stress coefficient, a high voltage can be easily generated in strained F-AlN sheet as shown in the schematic diagram of Fig. 5(b). Such strain-induced voltage can be evaluated as

$$V = \frac{\Delta P(\varepsilon)}{\pi \varepsilon_0} ln\left(\frac{L}{b}\right)$$

[36], where $\Delta P(\varepsilon)$ is the polarization change in the sample under the strain of ε, ε_0 is the vacuum dielectric constant ($\approx 8.854 \times 10^{-12} F/m$), L is the distance between two parallel line charges, and b is the effective radius of the lines, which is assumed to be the lattice constant of 3.24 Å along the y-direction (i.e. the zigzag orientation). When a 1% x-directional strain is applied across a 1 μm F-AlN sample, the voltage is estimated to be 3.19 V by this formula. This value is one order of magnitude larger than that in the H/F co-adsorbed graphene sheet under the same condition (0.2 V)[36]. Thus, utilizing the large piezoelectric stress coefficient e_{11}, higher voltage could be generated in the strained F-AlN sheet than the graphene derivatives. The voltage is controlled by applying strains to the piezoelectric parts, which would drive the flow of electrons in the external circuit and produce the current output. Therefore, the F-AlN sheet is a promising candidate for the nanogenerators and piezotronic transistors[72].

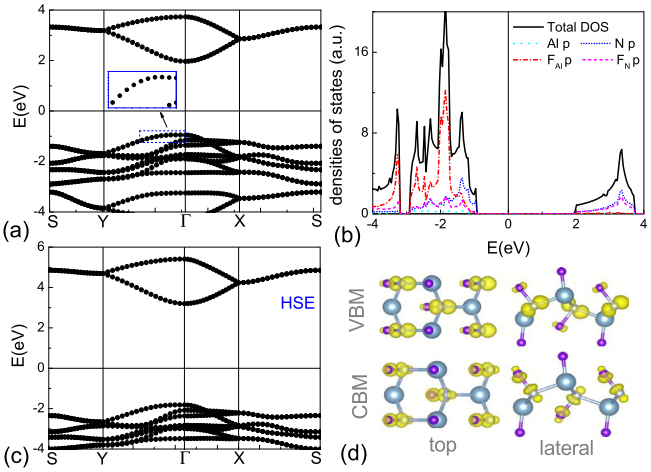

Fig. 6 (a) The PBE band structure and (b) total and partial DOSs of F-AlN sheet. (c) The HSE band structures, and (d) partial charge densities for the VBM and CBM of F-AlN sheet.

Electronic and Magnetic Properties

The band structure of 2D F-AlN sheet is depicted in Fig. 6(a), which exhibits an indirect-band-gap semiconducting feature. The conduction band minimum (CBM) is at the Γ point, while the valence band maximum (VBM) locates in the Γ −Y line. The partial density of states (PDOSs) analysis shows the top valence band mainly originates from the N atoms, while the bottom conduction band is contributed by the N and F p ones together. This is consistent with the partial charge densities of VBM and CBM in Fig. 6, which denotes the in-plane N p_x orbitals make up of the VBM while the N-F antibonding states compose the CBM mainly. It would be noticed that the top valence band is rather flat around the Γ point. As a result, the energy difference between the indi-

rect band gap and the direct one at Γ point is very small, which is merely 6 meV. Thus, the F-AlN sheet can be regarded as a quasi-direct-band-gap semiconductor, whose direct/indirect band gap is 2.92/2.91 eV by the PBE calculation. The hybrid HSE calculation obtains a similar band structure for F-AlN sheet except for the larger direct/indirect gap of 5.019/5.017 eV as shown in Fig. 6(b). As a comparison, we also calculate the pristine AlN sheet, which has a direct/indirect band gap of 5.47/4.49 eV from the HSE calculation. This demonstrates that the fluorination on AlN sheet decreases its direct band gap by 8% while increases the indirect one by 12%.

Although the 2D F-AlN sheet is a nonmagnetic system, peculiar magnetic properties can be achieved in its one-dimensional (1D) nanoribbons. As shown in Fig. 7, both the zigzag and armchair F-AlN nanoribbons (zF-AlNNRs and aF-AlNNRs) are investigated in the work. The initial configurations are adopted as the ones directly cut from the 2D form, which keep the ratio of F:AlN=1:1 as shown in Fig. 7(a). After full relaxation, in the aF-AlNNRs, the F-Al and F-N bonds at the edges are titled towards the outside of the nanoribbon as shown in Fig. 7(b). While in the zF-AlNNRs, a noticeable structural reconstruction occurs at the Al side edge. As marked in Fig. 7(c), the edge Al-N zigzag line bends downward, and one F atom, which originally connects to the next-to-edge N atom, is transferred to Al edge one. Since the Al-F bond is more energetically favourable than the N-F one[45], zigzag edges gain an energy of 0.63 eV/ Å from this reconstruction, which greatly enhances the edge stability of zF-AlNNRs. Figure 7(d) displays the edge energies of zF-AlNNRs and aF-AlNNRs as a function of ribbon width. Here, the edge energy of nanoribbons are calculated as $E_{edge} = (E_{F-AlNNR} - nE_{F-AlN})/2L$, in which $E_{F-AlNNR}$ is the total energy of 1D nanoribbon, E_{F-AlN} is the energy of corresponding 2D F-AlN sheet per formula unit, n is the number of formula unit for F-AlNNRs, and L is the edge length along the ribbon direction. The factor of 2 accounts for the two edges in nanoribbons. It shows that for the aF-AlNNRs the E_{edge} quickly converges to about 0.60 eV/Å, while for the zF-AlNNRs, the E_{edge} increases gradually and reaches a value of about 0.4 eV/Å for wide ribbons. These edge energies are lower than the corresponding values of pristine AlN (0.83 and 0.68 eV/Å in our calculations), graphene (1.31 and 0.98 eV/Å)[73], and BN (1.18 and 0.76 eV/Å)[74] nanoribbons, indicating the stronger edge stabilities of F-AlNNRs.

Besides the edge energy, the formation energies E_f of F-AlNNRs, which are defined as $E_f = E_{F-AlNNRs} - n_{AlN}E_{2D-AlN} - n_F E_{F_2}/2$, are also calculated to evaluate the energetic stabilities of F-AlN nanoribbons. Here, $E_{F-AlNNRs}$ is the total energy of the F-AlN nanoribbon, E_{2D-AlN} and E_{F2} are the corresponding energies of AlN sheet and free F_2 molecule, respectively. n_{AlN} is the number of AlN pairs in the nanoribbons, and n_F is the number of F atoms. Figure 7(e) depicts the formation energies of zigzag and armchair F-AlNNRs as a function of the ribbon width. It can be seen that all of these F-AlN nanoribbons possess negative E_f values, which indicates that the formation of F-AlNNRs is an exothermic process with an energy gain from the fluorination. For the zigzag nanoribbons, the E_f values are insensitive to the ribbon width, which are around -2.14 eV/F. While for the armchair nanoribbons, the E_f values decrease monotonically with the increasing ribbon width, which converge to -2.11 eV/F at the width of N_a = 15 as shown in Fig. 7(e). These E_f values of F-AlNNRs are still larger than that of F-AlN sheet (-2.206 eV/F in Tab. 1), which suggest it requires extra energies to form the F-AlN nanoribbons from 2D F-AlN sheet. This result is consistent with the obtained positive edge energies of nanoribbons in Fig. 7(d). It would be noted that the zigzag nanoribbons have more negative formation energies and lower edge energies than armchair ones, indicating they would be more possibly fabricated in the experiments.

Figure 8(a) displays the non-spin-polarized band structure and density of states (DOSs) for zF-AlNNRs at the width of $N_z = 6$. Different from the F-AlN sheet, this 6-zF-AlNNR exhibits a metallic behaviour, which stems from the polar discontinuity across the zigzag nanoribbon[75,76]. There are two flat bands crossing the Fermi level, inducing a large DOS peak. According to the Stoner criterion[77], it will lead to a spontaneous spin-polarization in the zF-AlNNRs. Through a spin-polarized calculation, we find that the ferromagnetic (FM) state is the ground magnetic state of 6-zF-AlNNR, which is 0.01 and 0.55 eV more stable than the antiferromagnetic (AFM) and nonmagnetic (NM) states, respectively. Besides the N_z=6 case, all the other zF-AlNNRs are also in favour of the FM state. For example, in the narrower 4-zF-AlNNR and wider 8-zF-AlNNRs, the energy differences between FM and AFM states are still about 0.01 eV, and the energy differences between FM and NM states become 0.64 and 0.48 eV, respectively. It would be noted that the preference of FM state is a common phenomenon for the N-induced magnetism. Previous studies have reported that the FM coupling is more stable than the AFM one in the bare N edges of AlN and BN nanoribbons[21,78]. Here, since the magnetism of zF-AlNNRs is also related to N atoms, the robust ferromagnetism can be expected in these zF-AlNNRs.

The corresponding distribution of spin charge density is depicted in Fig. 8(d), which shows that the magnetism is mainly contributed by the N atoms at the edges. The total magnetic moment is 2 μ_B, for which the N_1, N_2 and N_6 atoms contribute an atomic moment of 0.20, 0.86 and 0.54 μ_B, respectively. Interestingly, the 6-zF-AlNNR presents a half-metallic characteristic with the spin up channel semiconducting and the spin down one metallic as shown in Fig. 8(b). The half-metallicity is confirmed by the calculated total DOSs at the FM ground state. As shown in Fig. 8(b), in the spin up channel, the DOSs is zero at the Fermi level with an energy gap of 2.77 eV, while there is a finite DOSs at the Fermi level in the spin down channel, causing a half-metallic feature in the whole system. Thus, the nanoribbon is only con-

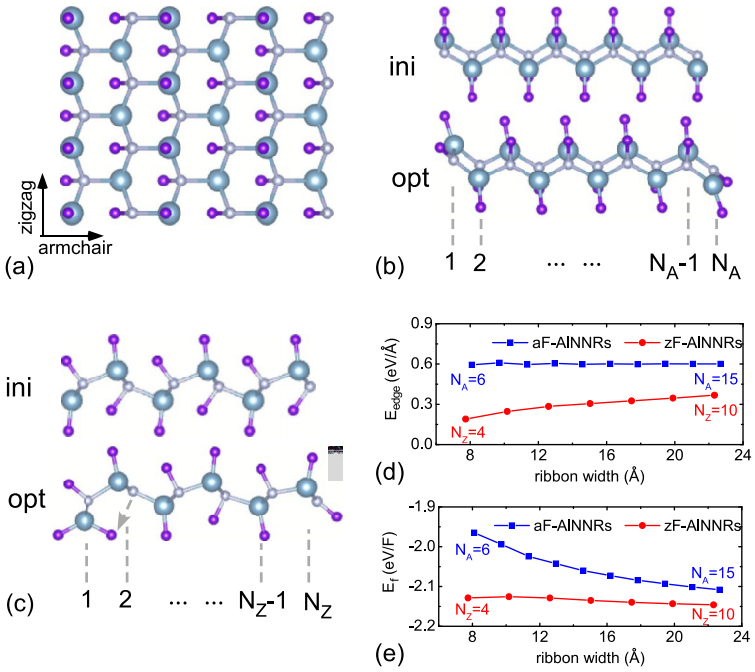

Fig. 7 (a) The top view of F-AlN sheet, from which the zigzag and armchair F-AlN nanoribbons can be obtained by directly cutting the sheet along the zigzag and armchair directions, respectively. (b) The initial and optimized structures of 10-aF-AlNNR. (c) The initial and optimized structures of 6-zF-AlNNR. (d) The edge energies and (e) formation energies of the zF-AlNNRs and aF-AlNNRs as a function of the ribbon width.

ductive for the spin down electrons, which leads to a 100% spin polarization. The half-metal gap, which is determined by the energy difference between the Fermi level and the VBM of spin up channel, is 0.22 eV for the 6-zF-AlNNR. Such value is much bigger than the thermal fluctuation at 300K (about 0.026 eV), which is large enough for the room temperature operation. The half-metallicity of 6-zF-AlNNR is also confirmed by the HSE calculation as shown in Fig. 8(c), which obtains a larger half-metal gap of 0.66 eV. Beside that, we find the half-metallicity of zF-AlNNRs is independent on the ribbon width. All the investigated N_z-zF-AlNNRs ($N_z = 4-10$), are half-metals as shown in Figs. 8(e) and (f), which indicates the zigzag F-AlN nanoribbons are intrinsic half-metallic nanomaterials.

Different from the zigzag ones, the aF-AlNNRs are semiconductors as shown in Figs. 9(a) and (b). For the 10-aF-AlNNR, a direct band gap of 1.61 (3.48) eV is obtained in the PBE (HSE) calculation, for which both the VBM and CBM locate at the Γ point. The semiconducting property is in accordance with the DOSs of system as depicted in Fig. 9(a). For the occupied states, there is a sharp DOSs peak at about -0.8 eV below the Fermi level, which arises from the nearly dispersonless feature of the top valence band. Whereas for the unoccupied states, the DOSs just above the Fermi level spans in a wide energy range of [0.8, 3] eV, which is attributed to the delocalized character of the bottom conduction bands. The corresponding partial charge densities in Fig. 9 (b) shows that the VBM is localized at the edge N-F bonds, while the CBM is distributed in the middle region of the nanoribbon. Thus, the band gaps of aF-AlNNRs will be modulated by the ribbon width. According to the quantum confinement effect, narrower aF-AlNNRs will possess larger band gaps, while the wider nanribbons have smaller ones. The data in Fig. 9 obeys this rule well. When the width $N_a \geq 14$, the PBE (HSE) calculation obtains a converged band gap of about 1.5 (3.4) eV for the aF-AlNNRs, which is smaller than the 2D value of 2.91 (5.02) eV. The reduced band gap of aF-AlNNRs is attributed to the edge states located in the fundamental gap of F-AlN sheet. Due to the localization of the edge states, the top valence bands from them are rather flat as shown in Fig. 9(a). If the Fermi level can be adjusted into these flat bands, it will provide a potential route to achieve half-metallicity in the aF-AlNNRs[79]. To this end we perform some test calculations on the 10-aF-AlNNR with extra positive charges of 0.25−1.0 $+e$/supercell, which correspond to the hole concentrations of 3.3×10^{13} ∼$1.3\times10^{14}/cm^{-2}$. As shown in Fig. 9(d), the hole-doped 10-aF-AlNNR successfully turns to a half-metal. For the 0.25, 0.5, 0.75 and 1.0 hole-doped cases, their half-metal gaps are 0.21, 0.40, 0.30, and 0.12 eV, respectively. Thus, although the aF-AlNNRs are not intrinsically half-metallic, they can be altered to half metals through hole doping, which induces tun-

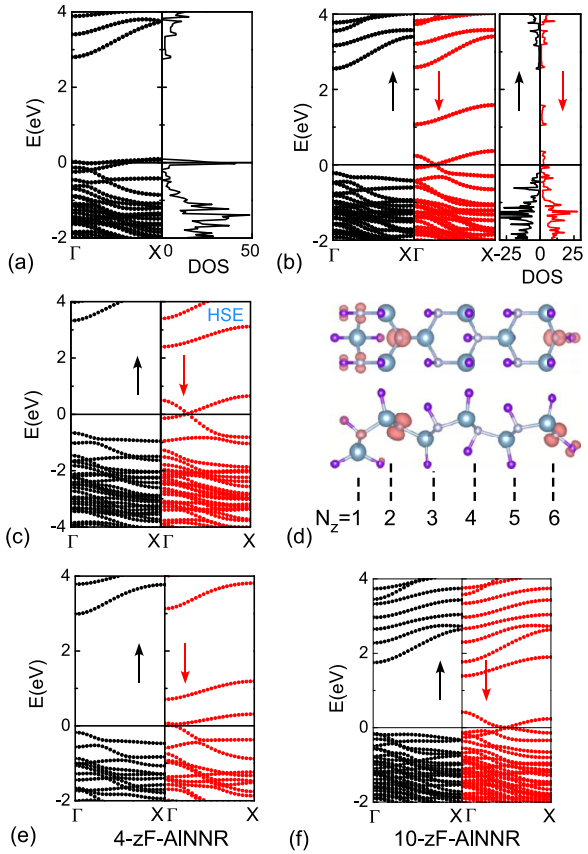

Fig. 8 (a) The NM band structure and DOSs of the 6-zF-AlNNR. (b) The FM band structure and DOSs of 6-zF-AlNNR by PBE calculations. (c) The HSE band structure of 6-zF-AlNNR. (d) The spin charge density distribution of 6-zF-AlNNR at the FM state. The PBE band structures are also plotted for (e) 4-zF-AlNNR and (f) 10-zF-AlNNR.

able half-metal gaps in the armchair nanoribbons.

4 Conclusion

In summary, we have performed a first-principles study on the structural, mechanical, piezoelectric and electronic properties of fluorinated AlN nanosheet and nanoribbons. We find that unlike the fluorinated graphene and BN sheets, the boat conformation is the most stable structure for the F-AlN sheet, for which the common chair conformation becomes unfavorable and dynamically unstable. Comparing to the pristine AlN sheet, the fluorination brings a softer mechanical character with a remarkable anisotropy in the Young's modulus and Possion ratio. More interestingly, the F-AlN sheet shows an enhanced piezoelectric performance, whose piezoelectric coefficients, especially the d_{11} and e_{11} ones, are larger than the values of hexagonal group III-V, group-III monochalcogenide, and transition metal dichalcogenide nanosheets. Utilizing such large e_{11} value, the generated voltage in the strained F-AlN sheet is an order of magnitude higher than that in the graphene derivatives. Comparing to the indirect-band-gap feature in pristine AlN system, the F-AlN sheet turns to a quasi-direct-band-gap semiconductor, while its armchair nanoribbons possess direct band gaps. The zigzag F-AlN nanoribbons exhibit an intrinsically half-metallic behaviour, in which the half-metal gaps are large enough for the room-temperature operation, and the hole-doped armchair ones can also be converted to half-metals, which have tunable band gaps depending on the doping concentration. Our study demonstrates the fluorinated AlN nanostructures possess promising piezoelectricity and intriguing half-metallicity, which are useful for the practical applications in nano-sized piezotronic and spintronic devices.

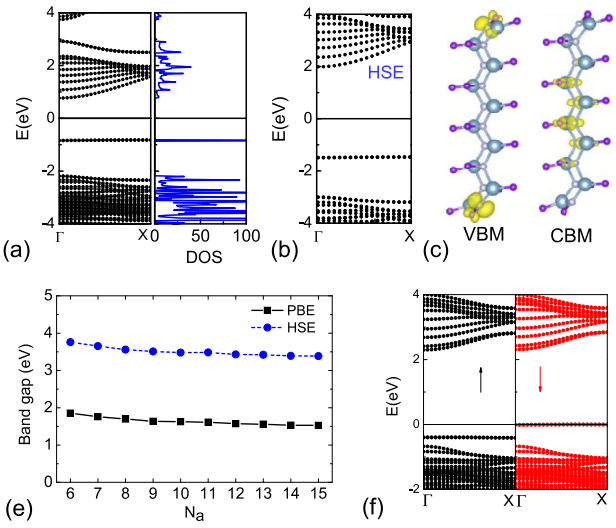

Fig. 9 (a) The band structure and DOSs of 10-aF-AlNNR by the PBE calculations. (b) The HSE band structures of 10-aF-AlNNR. (c) The partial charge densities for the VBM and CBM of 10-aF-AlNNR. (d) Variation of band gap as a function of armchair lines for the N_a-aF-AlNNRs. (e) The band structures of 10-aF-AlNNR with additional 0.5 hole in it. The black and red dots in the band structure represent the spin up and down electrons, respectively.

Acknowledgements

Authors acknowledge the supports from Zhejiang Provincial Natural Science Foundation of China (LY15A040008), National Natural Science Foundation of China (11474081). Some calculations are performed on the Shanghai Supercomputer Center in China.

References

1 A. K. Geim and K. S. Novoselov, *Nat. Mater.*, 2007, **6**, 183–191.

2 A. H. Castro Neto, F. Guinea, N. M. R. Peres, K. S. Novoselov and A. K. Geim, *Rev. Mod. Phys.*, 2009, **81**, 109–162.

3 M. Xu, T. Liang, M. Shi and H. Chen, *Chem. Rev.*, 2013, **113**,

3766–3798.
4 M. Osada and T. Sasaki, *Adv. Mater.*, 2012, **24**, 210–228.
5 X. Zhang, Z. Liu and S. Hark, *Solid State Commun.*, 2007, **143**, 317–320.
6 O. Landré, V. Fellmann, P. Jaffrennou, C. Bougerol, H. Renevier, A. Cros and B. Daudin, *Appl. Phys. Lett.*, 2010, **96**, 061912.
7 Q. Wu, N. Liu, Y. Zhang, W. Qian, X. Wang and Z. Hu, *J. Mater. Chem. C*, 2015, **3**, 1113–1117.
8 L. P. Wang, E. Ginsburg, F. Gerfers, D. Samara-Rubio, B. Weinfeld, Q. Ma, V. Rao and M. Y. He, 5th IEEE Conference on Sensors, 2006, pp. 10–13.
9 M.-A. Dubois and P. Muralt, *Appl. Phys. Lett.*, 1999, **74**, 3032–3034.
10 N. Sinha, G. E. Wabiszewski, R. Mahameed, V. V. Felmetsger, S. M. Tanner, R. W. Carpick and G. Piazza, *Appl. Phys. Lett.*, 2009, **95**, 053106.
11 P. Tsipas, S. Kassavetis, D. Tsoutsou, E. Xenogiannopoulou, E. Golias, S. A. Giamini, C. Grazianetti, D. Chiappe, A. Molle, M. Fanciulli and A. Dimoulas, *Appl. Phys. Lett.*, 2013, **103**, 251605.
12 V. Mansurov, T. Malin, Y. Galitsyn and K. Zhuravle, *J. Cryst. Growth*, 2015, **428**, 93 – 97.
13 C. Bacaksiz, H. Sahin, H. D. Ozaydin, S. Horzum, R. T. Senger and F. M. Peeters, *Phys. Rev. B*, 2015, **91**, 085430.
14 A. K. Singh, H. L. Zhuang and R. G. Hennig, *Phys. Rev. B*, 2014, **89**, 245431.
15 S. Valedbagi, A. Fathalian and S. Mohammad Elahi, *Opt. Commun.*, 2013, **309**, 153–157.
16 J. de Almeida, E.F., F. de Brito Mota, C. de Castilho, A. Kakanakova-Georgieva and G. Gueorguiev, *Eur. Phys. J. B*, 2012, **85**, 48.
17 P. Liu, A. D. Sarkar and R. Ahuja, *Comp. Mater. Sci.*, 2014, **86**, 206–210.
18 C. W. Zhang, *J. Appl. Phys.*, 2012, **111**, 043702.
19 T. Xie, Y. Lin, G. Wu, X. Yuan, Z. Jiang, C. Ye, G. Meng and L. Zhang, *Inorg. Chem. Commun.*, 2004, **7**, 545–547.
20 Q. Chen, R. Song, C. Chen and X. Chen, *Solid State Commun.*, 2013, **172**, 24–28.
21 H. X. Luan, C. W. Zhang and S. S. Yan, *EPL*, 2013, **103**, 37009.
22 A. Lopez-Bezanilla, P. Ganesh, P. R. Kent and B. G. Sumpter, *Nano Res.*, 2014, **7**, 63–70.
23 X. J. Du, Z. Chen, J. Zhang, Z. R. Ning and X. L. Fan, *Superlattices Microstruct.*, 2014, **67**, 40–46.
24 T.-t. Sun, Y.-x. Wang, Z. Chen and X.-j. Du, *Comp. Mater. Sci.*, 2014, **92**, 372–376.
25 X.-J. Du, Z. Chen, J. Zhang, Z.-R. Ning and X.-L. Fan, *J. Alloys Com.*, 2014, **586**, 176–179.
26 V. Georgakilas, M. Otyepka, A. B. Bourlinos, V. Chandra, N. Kim, K. C. Kemp, P. Hobza, R. Zboril and K. S. Kim, *Chem. Rev.*, 2012, **112**, 6156–6214.
27 J. E. Johns and M. C. Hersam, *Acc. Chem. Res.*, 2013, **46**, 77–86.
28 D. C. Elias, R. R. Nair, T. M. G. Mohiuddin, S. V. Morozov, P. Blake, M. P. Halsall, A. C. Ferrari, D. W. Boukhvalov, M. I. Katsnelson, A. K. Geim and K. S. Novoselov, *Science*, 2009, **323**, 610–613.
29 M. Inagaki and F. Kang, *J. Mater. Chem. A*, 2014, **2**, 13193–13206.
30 R. R. Nair, W. Ren, R. Jalil, I. Riaz, V. G. Kravets, L. Britnell, P. Blake, F. Schedin, A. S. Mayorov, S. Yuan, M. I. Katsnelson, H.-M. Cheng, W. Strupinski, L. G. Bulusheva, A. V. Okotrub, I. V. Grigorieva, A. N. Grigorenko, K. S. Novoselov and A. K. Geim, *Small*, 2010, **6**, 2877–2884.
31 M. Du, X. Li, A. Wang, Y. Wu, X. Hao and M. Zhao, *Angew. Chem. Int. Ed.*, 2014, **53**, 3645–3649.
32 J. Zhou, Q. Wang, Q. Sun, X. S. Chen, Y. Kawazoe and P. Jena, *Nano Lett.*, 2009, **9**, 3867–3870.
33 D. K. Samarakoon, Z. Chen, C. Nicolas and X.-Q. Wang, *Small*, 2011, **7**, 965–969.
34 J. Zhou, Q. Wang, Q. Sun and P. Jena, *Phys. Rev. B*, 2010, **81**, 085442.
35 H. Y. Liu, Z. F. Hou, C. H. Hu, Y. Yang and Z. Z. Zhu, *J. Chem. Phys. C*, 2012, **116**, 18193–18201.
36 M. T. Ong, K.-A. N. Duerloo and E. J. Reed, *J. Phys. Chem. C*, 2013, **117**, 3615–3620.
37 Y. Yang, W. Ren and L. Bellaiche, *Phys. Rev. B*, 2014, **89**, 245439.
38 W.-Z. Yu, J.-A. Yan and S.-P. Gao, *Nanoscale Res. Lett.*, 2015, **10**, 351.
39 S. Tang and S. Zhang, *J. Chem. Phys. C*, 2011, **115**, 16644–16651.
40 S. Tang, J. Yu and L. Liu, *Phys. Chem. Chem. Phys.*, 2013, **15**, 5067–5077.
41 Y. Wang and S. Shi, *Solid State Commun.*, 2010, **150**, 1473–1478.
42 W. X. Zhang, T. Li, S. B. Gong, C. He and L. Duan, *Phys. Chem. Chem. Phys.*, 2015, **17**, 10919–10924.
43 C. W. Zhang and P. J. Wang, *Phys. Lett. A*, 2011, **375**, 3583–3587.
44 C. W. Zhang and F. B. Zheng, *J. Comput. Chem.*, 2011, **32**, 3122–3128.
45 C. W. Zhang and S. S. Yan, *J. Phys. Soc. Jpn.*, 2012, **81**, 044705.
46 S. S. Li, C. W. Zhang, R. W. Zhang, P. Li, F. Li, M. Yuan, M. J. Ren, W. X. Ji and P. J. Wang, *RSC Adv.*, 2014, **4**, 7500–7505.

47 A. Bhattacharya, S. Bhattacharya and G. P. Das, *Phys. Rev. B*, 2012, **85**, 035415.

48 Y. Ding and Y. Wang, *Appl. Phys. Lett.*, 2012, **100**, 083102.

49 G. Kresse and J. Furthmuller, *Comput. Mater. Sci.*, 1996, **6**, 15–50.

50 G. Kresse and J. Furthmuller, *Phys. Rev. B*, 1996, **54**, 11169–11186.

51 S. Grimme, J. Antony, S. Ehrlich and H. Krieg, *J. Chem. Phys.*, 2010, **132**, 154104.

52 S. Grimme, S. Ehrlich and L. Goerigk, *J. Comp. Chem.*, 2011, **32**, 1456–1465.

53 V. Blum, R. Gehrke, F. Hanke, P. Havu, V. Havu, X. Ren, K. Reuter and M. Scheffler, *Comput. Phys. Commun.*, 2009, **180**, 2175 – 2196.

54 A. Togo and I. Tanaka, *Scr. Mater.*, 2015, **108**, 1–5.

55 A. Togo, F. Oba and I. Tanaka, *Phys. Rev. B*, 2008, **78**, 134106.

56 S. Balendhran, S. Walia, H. Nili, S. Sriram and M. Bhaskaran, *Small*, 2015, **11**, 640–652.

57 H. Şahin, M. Topsakal and S. Ciraci, *Phys. Rev. B*, 2011, **83**, 115432.

58 M. Noor-A-Alam, H. J. Kim and Y.-H. Shin, *Phys. Chem. Chem. Phys.*, 2014, **16**, 6575–6582.

59 E. Cadelano, P. L. Palla, S. Giordano and L. Colombo, *Phys. Rev. B*, 2010, **82**, 235414.

60 Y. Wang and Y. Ding, *Phys. Status Solidi RRL*, 2013, **7**, 410–413.

61 Q. Peng, X. J. Chen, S. Liu and S. De, *RSC Adv.*, 2013, **3**, 7083–7092.

62 E. Cadelano and L. Colombo, *Phys. Rev. B*, 2012, **85**, 245434.

63 M. N. Blonsky, H. L. Zhuang, A. K. Singh and R. G. Hennig, *ACS Nano*, 2015, **9**, 9885–9891.

64 M. M. Alyörük, Y. Aierken, D. Çakır, F. M. Peeters and C. Sevik, *J. Chem. Phys. C*, 2015, **119**, 23231–23237.

65 R. D. King-Smith and D. Vanderbilt, *Phys. Rev. B*, 1993, **47**, 1651–1654.

66 D. Vanderbilt and R. D. King-Smith, *Phys. Rev. B*, 1993, **48**, 4442–4455.

67 W. Li and J. Li, *Nano Res.*, 2015, **8**, 3796–3802.

68 K.-A. N. Duerloo, M. T. Ong and E. J. Reed, *J. Phys. Chem. Lett.*, 2012, **3**, 2871–2876.

69 R. Fei, W. Li, J. Li and L. Yang, *Appl. Phys. Lett.*, 2015, **107**, 173104.

70 R. Bechmann, *Phys. Rev.*, 1958, **110**, 1060–1061.

71 H. Ogi, N. Nakamura, K. Sato, M. Hirao and S. Uda, *IEEE Trans. Ultrason., Ferroelect., Freq. Contr.*, 2003, **50**, 553–560.

72 Y. Liu, Y. Zhang, Q. Yang, S. Niu and Z. L. Wang, *Nano Energy*, 2015, **14**, 257 – 275.

73 P. Koskinen, S. Malola and H. Häkkinen, *Phys. Rev. Lett.*, 2008, **101**, 115502.

74 R. Mukherjee and S. Bhowmick, *J. Chem. Theory Comput.*, 2011, **7**, 720–724.

75 M. Gibertini, G. Pizzi and N. Marzari, *Nat. Commun.*, 2014, **5**, 5157.

76 M. Gibertini and N. Marzari, *Nano Lett.*, 2015, **15**, 6229–6238.

77 E. C. Stoner, *Philos. Mag.*, 1924, **48**, 719.

78 F. Zheng, G. Zhou, Z. Liu, J. Wu, W. Duan, B. L. Gu and S. B. Zhang, *Phys. Rev. B*, 2008, **78**, 205415.

79 T. Cao, Z. Li and S. G. Louie, *Phys. Rev. Lett.*, 2015, **114**, 236602.

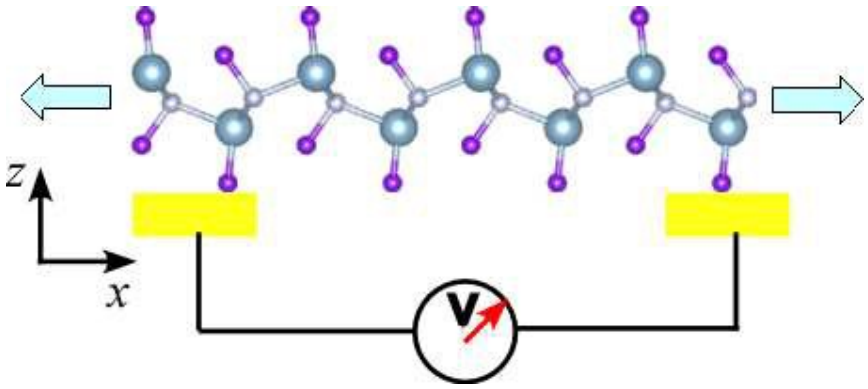

The fluorinated AlN nanosheets present an enhanced piezoelectric performance and the corresponding nanoribbons can exhibit an half-metallic behaviour.